solids

MDPI

Article

The Ni_3Al/Ni Interfacial Contribution to the Indentation Size Effect of Ni-Based Single-Crystal Superalloys

Zhiwei Zhang [1,2,*], Xingyi Zhang [1,2], Rong Yang [3], Jun Wang [3,*] and Chunsheng Lu [4]

[1] Department of Mechanics and Engineering Sciences, College of Civil Engineering and Mechanics, Lanzhou University, Lanzhou 730000, China
[2] Key Laboratory of Mechanics on Environment and Disaster in Western China, The Ministry of Education of China, Lanzhou University, Lanzhou 730000, China
[3] State Key Laboratory of Nonlinear Mechanics (LNM), Institute of Mechanics, Chinese Academy of Sciences, Beijing 100190, China
[4] School of Civil and Mechanical Engineering, Curtin University, Perth, WA 6845, Australia
* Correspondence: zhangzhiwei@lzu.edu.cn (Z.Z.); wangjun@lnm.imech.ac.cn (J.W.)

Abstract: Hardness decreases as indentation depth increases at both the nano- and micro-meter scales. By incorporating interfacial contributions, the indentation size effect can provide valuable information on the deformation behaviors of Ni-based single-crystal superalloys. In this paper, through experimental studies and atomistic simulations, we examine the indentation size effect and mechanical behaviors of Ni-based single-crystal superalloys. The results demonstrate that the indentation size effect, in conjunction with the Ni_3Al/Ni interfacial network, is effectively captured by a modified Nix–Gao model. Molecular dynamics simulations further reveal the underlying atomistic mechanisms and microstructural evolution during nanoindentation. These findings provide new insights into the deformation behavior of Ni-based single-crystal superalloys and support their wide applications in the aerospace industry.

Keywords: Ni-based single-crystal superalloys; indentation size effect; Ni_3Al/Ni interfaces; hardness; molecular dynamics

check for updates

Citation: Zhang, Z.; Zhang, X.; Yang, R.; Wang, J.; Lu, C. The Ni_3Al/Ni Interfacial Contribution to the Indentation Size Effect of Ni-Based Single-Crystal Superalloys. *Solids* **2024**, *5*, 580–592. https://doi.org/10.3390/solids5040039

Academic Editor: Timothy J. Prior

Received: 29 September 2024
Revised: 7 November 2024
Accepted: 12 November 2024
Published: 25 November 2024

Copyright: © 2024 by the authors. Licensee MDPI, Basel, Switzerland. This article is an open access article distributed under the terms and conditions of the Creative Commons Attribution (CC BY) license (https://creativecommons.org/licenses/by/4.0/).

1. Introduction

Over recent decades, nanoindentation experiments and atomistic simulations have been widely used to investigate the mechanical behaviors and plastic deformation mechanisms of materials at both nano- and micro-scale levels [1–4]. The indentation size effect, where hardness decreases with increasing indentation depth, is usually attributed to the accumulation of geometrically necessary dislocations and associated plastic gradients [5–8]. This effect also depends on the indenter shape, such as conical or spherical geometries [9,10]. The Nix–Gao model [11] has proven effective for predicting the indentation size effect in monocrystalline copper with conical indenters, and it has been further developed to elaborate the effect in other metals with spherical indenters [9,12–14]. However, nanoindentation at micro- and nano-scale sometimes deviates from the Nix–Gao model, suggesting that additional microstructural factors need to be incorporated when a sample does not conform to the continuous medium assumption [15–17].

Ni-based single-crystal superalloys are extensively applied in the aerospace industry due to their excellent thermodynamic properties [18–20]. These unique properties arise from a superlattice structure, consisting of the Ni matrix and Ni_3Al precipitate phases [21,22]. In line with convention in the literature on Ni-based single-crystal superalloys, the terms, precipitate and matrix, are used here, though the Ni_3Al phase is often larger than the Ni matrix. The Ni_3Al/Ni heterogeneous interfacial misfit dislocation network enables dislocations to be either absorbed or impeded, setting Ni-based superalloys apart from other single-crystal materials, especially during nanoindentation. Based on

force–depth curves derived from nanoindentation, mechanical properties like Young's modulus and hardness can be deduced. However, it remains challenging to correlate these properties with specific indentation sites, which can be in the Ni matrix, the Ni_3Al precipitate, or the interface. This makes the indentation size effect more complex, as it is closely tied to the indentation site and the resulting force–depth curve. Although transmission electron microscopy (TEM) and scanning electron microscopy (SEM) can help locate indentation sites, they do not capture the underlying microstructural evolution within the sample. Fortunately, molecular dynamics simulations can address this by linking force–depth curves with microstructural changes [23–25].

In previous studies, we employed nanoindentation simulations to investigate hardening effects from twin boundaries and stacking faults within the precipitation phase Ni_3Al of Ni-based superalloys [18]. Additionally, molecular dynamics simulations revealed dislocation reactions responsible for pop-in events during nanoindentation, with results validated by experiments and theoretical analysis [26]. However, to the best of our knowledge, research on the Ni_3Al/Ni interfacial contribution to the indentation size effect remains limited.

In this paper, we first characterized the microstructures of Ni-based single-crystal superalloys using TEM and SEM techniques. Then, nanoindentation was conducted to collect force–depth curves at specific sites within the Ni matrix, Ni_3Al precipitates, and the Ni_3Al/Ni interface, which were identified through SEM imaging post-indentation. The modified Nix–Gao model was subsequently fitted to the experimental data, incorporating the Ni_3Al/Ni interfacial contribution. Finally, molecular dynamics simulations were carried out to link the indentation size effect to microstructural evolution during nanoindentation.

2. Experiments

2.1. Materials, Specimen Preparation, and Structural Observation

Ni-based single-crystal superalloy cylinders, with a diameter of 1.5 cm and a length of 15 cm, were prepared for the experiments. Table 1 lists the chemical compositions of the superalloys. To prepare samples for nanoindentation and electron microscopy observation, the cylinder was sliced into uniform sections with a thickness of 0.1 cm using a diamond wire saw, ensuring consistent sample quality. The specimens were then electrochemically polished utilizing a direct-current power supply and an electrolyte solution consisting of sulfuric acid to deionized water in a 40:60 ratio at room temperature. The polished surfaces were carefully examined to confirm the absence of any significant work hardening layer or mechanical damage.

Table 1. Chemical composition of the Ni-based single-crystal superalloys.

Element	Ni	Co	W	Ta	Al	Cr	Mo	Re	Hf
wt.%	61.4	9	8	7.5	5.7	4.3	2	2	0.1

Before the nanoindentation procedure, the microstructural characteristics of the Ni-based single-crystal superalloys were analyzed via TEM (JEOL JEM-2100F, Japan) and SEM (ZEISS Supra-55, Germany). Thin foils for TEM observation were prepared by thinning and polishing sheets to a thickness of 50 μm, then punching them into 0.3 cm diameter disks, and finally perforating them in a twin-jet electro-polishing apparatus. This was performed with a solution of 5 vol.% perchloric acid and 95 vol.% alcohol at −45 °C and 65 V [27]. TEM imaging enabled detailed microstructural characterization of the superalloys, revealing Ni_3Al precipitates with cuboidal morphologies within the Ni matrix, with an average particle edge length of approximately 500 nm (see Figure 1a) [26].

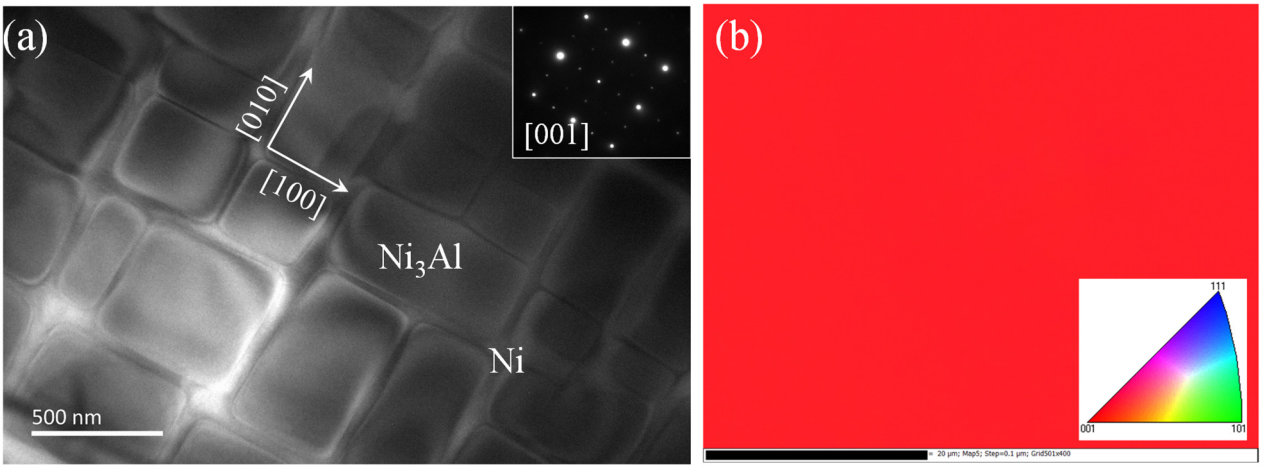


Figure 1. (**a**) TEM image of Ni_3Al precipitates and the Ni matrix. (**b**) EBSD crystallographic orientation map obtained via SEM.

The ZEISS Supra-55 SEM, equipped with electron backscattering diffraction (EBSD), was used to examine the crystalline orientations of the superalloy specimens. Samples for EBSD were first mechanically polished and subsequently electro-polished. Locating identical positions in TEM and SEM was challenging due to the absence of distinct surface markers. Therefore, EBSD images were collected from over 10 sites to ensure that the crystalline orientation of the Ni-based superalloys aligned along the [001] direction (see Figure 1b). SEM was further utilized to assess the surface indentation morphology of the superalloys following nanoindentation.

2.2. Nanoindentation Tests

Nanoindentation tests were conducted to assess the hardness and indentation size effect of Ni-based superalloys by using an Agilent Nano Indenter G200 system (DCMII Instruments). Indentations were made using a Berkovich indenter, with a 230 nm tip curvature radius, and the area function was identified through calibration on a fused silica standard specimen. All indentations were created at a constant strain rate of 0.05 s^{-1} by increasing the applied load proportionally with elapsed time (calculated as indentation speed divided by target depth). Continuous stiffness measurements were recorded during indentation to determine the hardness of the superalloys [28].

In addition, a series of continuous stiffness measurements were collected at a harmonic oscillation frequency of 75 Hz and a root mean square displacement amplitude of 2 nm, with samples held at target depths ranging from 30 to 400 nm, where unloading occurred at each measurement point. To prevent interference between adjacent indentations, arrays of over 30 indents were made at each depth with a 10 μm spacing. Data on indentation force and hardness as a function of depth were extracted to facilitate a detailed analysis of the indentation behavior.

3. Numerical Models and Methodology

3.1. Molecular Dynamics Models

The Ni-based single-crystal superalloy comprises a pure FCC Ni matrix and $L1_2$ Ni_3Al precipitates, resulting in lattice mismatch at the Ni_3Al/Ni interface. To create a coincidence site lattice on this misfit interface, a minimum of 66 Ni_3Al lattice units and 67 Ni lattice units must be relaxed to relieve stress caused by the lattice parameter discrepancy between Ni (3.52 Å) and Ni_3Al (3.573 Å) [29].

It is demonstrated that a misfit dislocation network forms at the Ni_3Al/Ni interface due to lattice mismatch, reducing internal strain energy and accommodating misfit strain [30]. As illustrated in Figure 2, there are three initial indentation configurations for sites at the Ni_3Al precipitate, the Ni matrix, and the Ni_3Al/Ni interface. These were modeled as cuboidal structures with dimensions of 23.6 × 23.6 × 23.6 nm^3 along the X-[010], Y-[001], and Z-[100] directions, containing ~1,180,000 atoms. A hemispherical diamond indenter, with a diameter of 12 nm containing ~34,000 atoms, was produced. During indentation, periodic boundary conditions were applied in the X and Y directions, while the upper surface was free for indentation, and the lower surface was fixed with an assigned thickness of 1.0 nm.

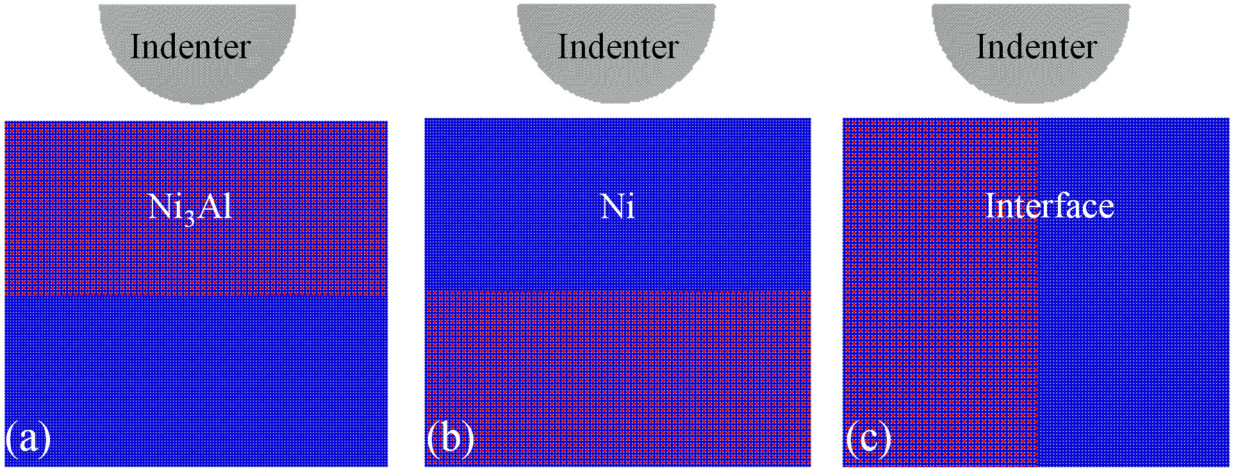


Figure 2. Molecular dynamics simulation configurations with nanoindentation sites at (**a**) Ni_3Al precipitate, (**b**) Ni matrix, and (**c**) Ni_3Al/Ni interface.

3.2. Potential Function and Methods

Molecular dynamics simulations were conducted utilizing the largescale atomic/molecular massively parallel simulator [31]. The atomic interaction between Ni_3Al and Ni was modeled using an embedded-atom potential function developed by Mishin [32]. In this potential, the total energy, U, of the system is represented by

$$U = \sum_{\substack{i,j \\ i \neq j}} V_{EAM}(r_{ij}) + \sum_i F(\overline{\rho_i}), \quad (1)$$

where $V_{EAM}(r_{ij})$ is a pair potential function of the distance r_{ij} between atoms i and j, F is the embedding energy of atom i, and $\overline{\rho_i}$ is the electron density, which is defined as

$$\overline{\rho_i} = \sum_{i \neq j} g_j(r_{ij}), \quad (2)$$

where $g_j(r_{ij})$ is the electron density of atom j.

Here, it is worth noting that such a potential is built up by fitting to data from experiments and first principles calculations. It can accurately depict the lattice structure, mechanical properties, energetics of point defects, dislocations, and planar faults in Ni_3Al and Ni [33].

To simulate the interaction between the diamond indenter and Ni_3Al/Ni substrate, a two-body Lennard–Jones potential was used:

$$E = 4 \sum_{\substack{i,j \\ i \neq j}} \varepsilon_{ij} \left[\left(\frac{\sigma_{ij}}{r_{ij}} \right)^{12} - \left(\frac{\sigma_{ij}}{r_{ij}} \right)^{6} \right], r_{ij} < r_0, \quad (3)$$

where ε_{ij} is the cohesive energy, σ_{ij} is the equilibrium distance, and r_0 is the cutoff distance. For the C–Ni interaction, these values are 2.31×10^{-4} eV, 0.2852 nm, and 0.8 nm, respectively; for C–Al, they are 3.15×10^{-4} eV, 0.2976 nm, and 0.8 nm [34,35].

The atomistic simulations were conducted using a method of integrating Newton's laws of motion, which was applied to each atom in a temporal interval of 1 fs. Initial configurations were relaxed by energy minimization, followed by 50 ps of equilibrium at 300 K. The indentation load was then applied to the Ni_3Al precipitate, Ni matrix, and Ni_3Al/Ni interface (see Figure 2) at a speed of 10 m s^{-1} with a step increment of 0.05 nm. The maximum indentation depth was set at 4.0 nm, smaller than the indenter's diameter (12 nm). Deformations in the Ni_3Al/Ni substrate were identified and visualized with the software OVITO 3.0.0-dev592 [36].

4. Results

4.1. Pop-In Events and Indentation Behaviors

Figure 3a shows two typical force–depth curves for indentations made on the Ni_3Al/Ni interface and Ni_3Al precipitate. The indentations are oriented perpendicular to the crystal surface of the (001) plane, with a maximum depth of 30 nm. Figure 3b presents the corresponding hardness–indentation depth curves, illustrating that the indentation force–depth and hardness–depth values at Ni_3Al/Ni interface (Figure 3c) are lower than those observed for the Ni_3Al precipitate (Figure 3d). In addition, two types of pop-in events appear in the loading sequence: the first pop-in (indicated by black arrows in Figure 3a) and subsequent pop-in events (green arrows in Figure 3a). The initial pop-in event exhibits the largest displacement burst, corresponding to a noticeable drop in hardness (see Figure 3b). It is worth noting that, however, the displacement burst of the first pop-in at the Ni_3Al/Ni interface is smaller than that at the Ni_3Al precipitate. When the maximum indentation depth increases to 50 nm, similar patterns are observed (see Figure 4a,b). Here, the hardness H is calculated by

$$H = \frac{F}{A}, \quad (4)$$

where F and A represent the force exerted by an indenter and the contact area between the indenter and a sample. The latter is

$$A = \sum_{n=0}^{8} C_n h_c^{\frac{1}{2^{n+1}}}, \quad (5)$$

where the contact depth $h_c = h_m - \varepsilon \frac{F_m}{\alpha m (h_m - h_f)^{m-1}}$, with h_f, h_m, and F_m being the residual depth, maximum indentation depth, and maximum force, respectively. The parameter $\varepsilon = 0.75$ accounts for the geometry of the Berkovich indenter, incorporating the influence of the tip radius and the pyramid edge radii. SEM images illustrate that a maximum indentation depth of 50 nm is the limit for distinguishing between indentations on the Ni_3Al precipitate and the Ni_3Al/Ni interface, as this depth brings the SEM morphology boundary close to the edge of the Ni_3Al precipitate (see Figure 4c,d).

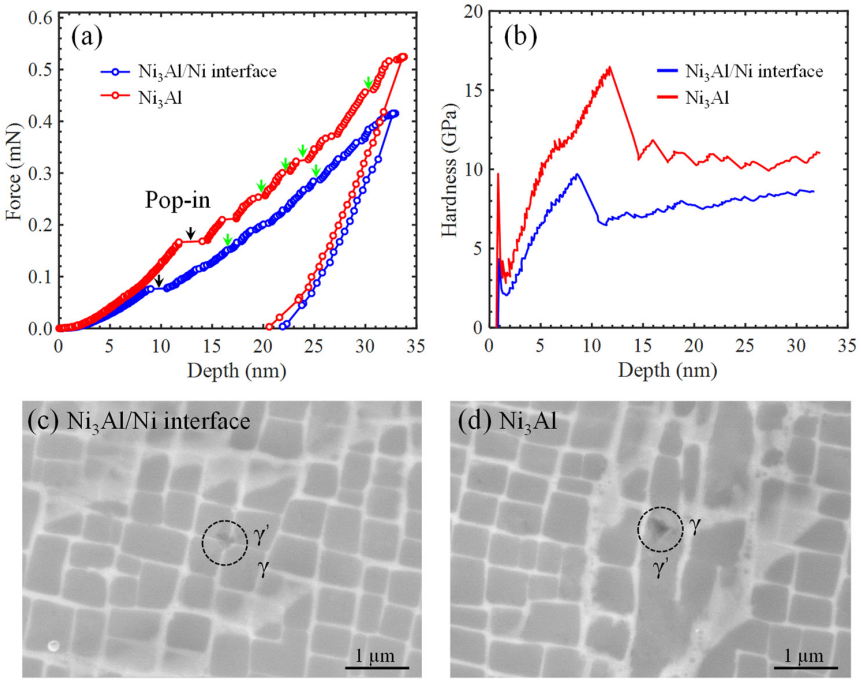


Figure 3. (**a**) The indentation force–depth and (**b**) hardness–depth curves at a maximum indentation depth of 30 nm, with black and green arrows indicating the initial and subsequent pop-in events, respectively. Microstructural characteristics and indentation morphologies show that indentations occur on (**c**) the Ni_3Al precipitate phase, γ', and (**d**) the Ni matrix phase, γ.

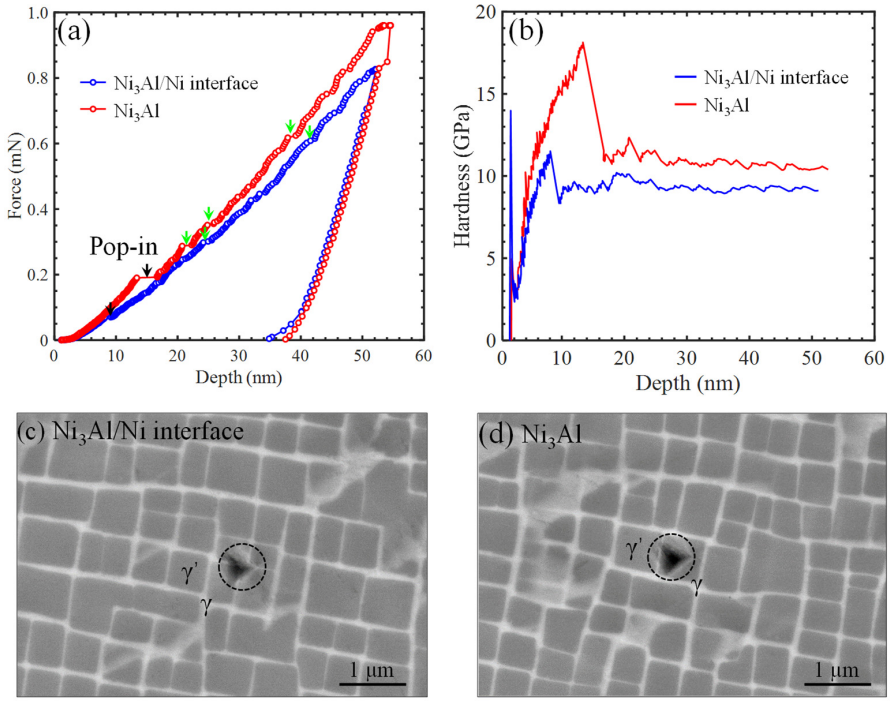


Figure 4. (**a**) The indentation force–depth and (**b**) hardness–depth curves at a maximum indentation depth of 50 nm, with black and green arrows marking the first and subsequent pop-in events, respectively [26]. SEM images show indentations made on (**c**) the Ni_3Al precipitate phase, γ', and (**d**) the Ni matrix phase, γ.

Beyond a maximum indentation depth of 50 nm, a discrepancy in the force/hardness curves at shallower depths becomes evident (see insets in Figure 5). Because the size of the

indentation morphology exceeds that of a single Ni_3Al precipitate (Figure 6), it is difficult to directly associate the discrepancy with the initial indentation site. However, useful information can be extracted from the hardness–depth curves. Specifically, all hardness–depth curves display a peak at an approximately 10 nm indentation depth, corresponding to the first pop-in event on force–depth curves. The higher the peak value is, the closer the indentation site is to the Ni_3Al precipitate center. Conversely, the indentation site is closer to the center of the Ni matrix. In addition, hardness is independent of indentation sites as depth surpasses ~100 nm. SEM images reveal that at maximum indentation depths exceeding 70 nm, the indentation morphology spans multiple Ni_3Al precipitates and Ni_3Al/Ni interfaces (Figure 6). Therefore, the hardness–depth curves beyond ~100 nm reflect the response of the entire Ni-based superalloy superlattice structure.

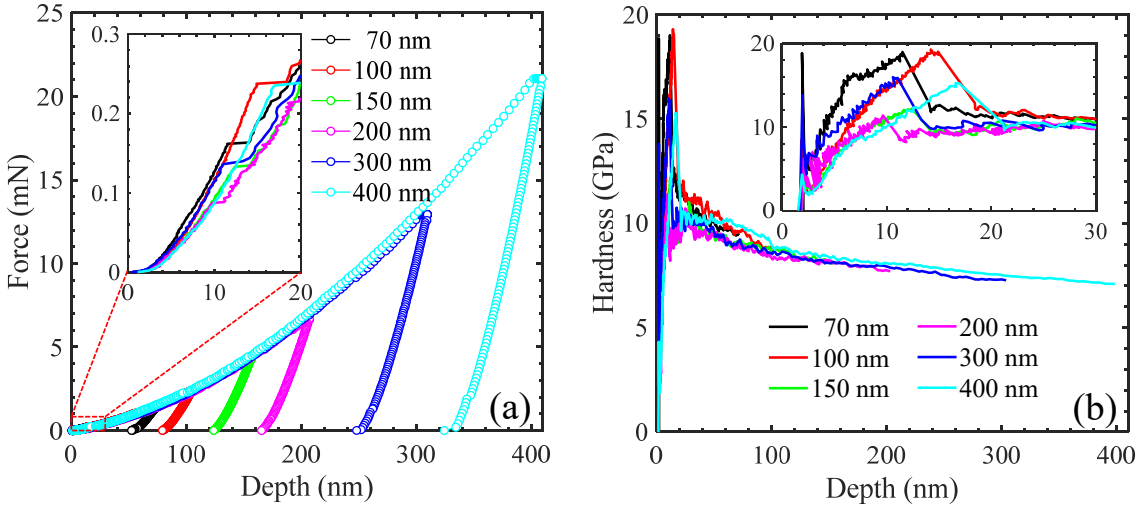


Figure 5. (**a**) The indentation force–depth and (**b**) hardness–depth relationships for maximum indentation depths ranging from 70 to 400 nm.

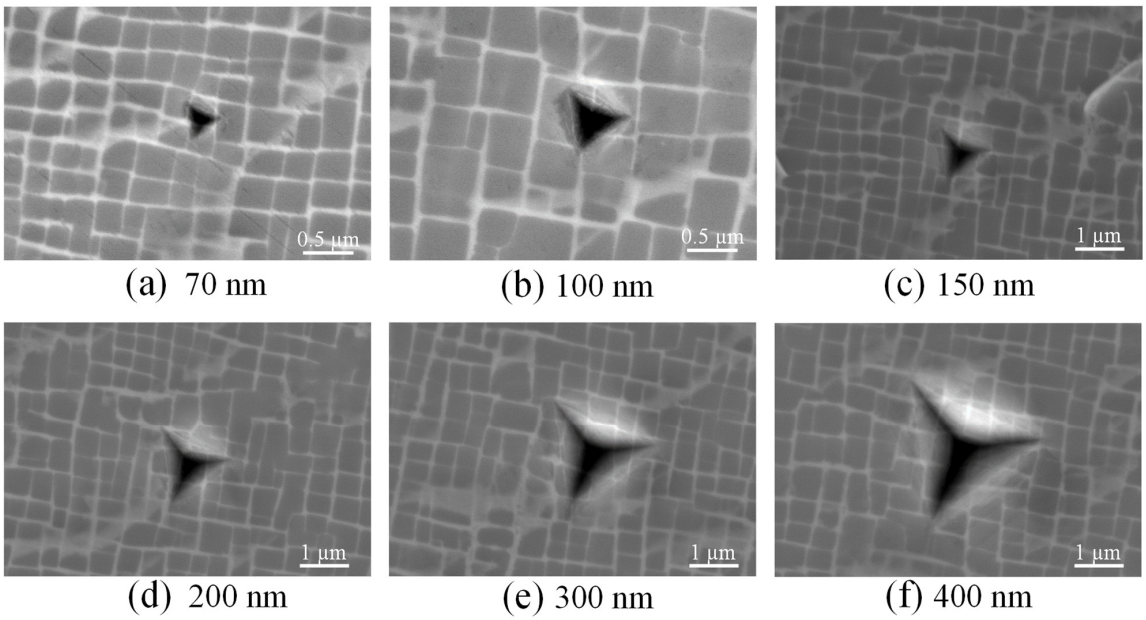


Figure 6. Microstructural characteristics and indentation morphologies with the maximum indentation depths of (**a**) 70, (**b**) 100, (**c**) 150, (**d**) 200, (**e**) 300, and (**f**) 400 nm.

4.2. Indentation Size Effect

As shown in Figure 7a, hardness decreases with increasing indentation depth, from 10.34 GPa at 30 nm to 6.98 GPa at 400 nm. Hardness fluctuations are more pronounced at shallower depths due to variation in initial indentation sites, such as the Ni matrix, Ni_3Al precipitate, and Ni_3Al/Ni interface. Beyond 100 nm, these fluctuations lessen (Figure 7a), reflecting the cumulative response of the superlattice structure of Ni-based single-crystal superalloys. When plotting H^2 versus h^{-1} (Figure 7b), a strong linear relationship emerges for depths beyond 70 nm, suggesting that the Nix–Gao model [11] reliably predicts the $H - h$ relationship. However, at depths below 70 nm, the experiment data deviate from those of the Nix–Gao model, suggesting that the Ni_3Al/Ni interfacial contribution should be considered.

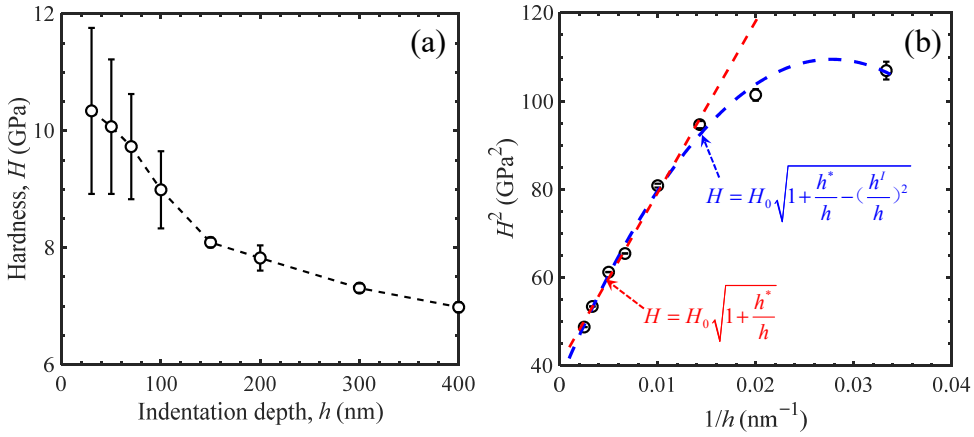


Figure 7. (**a**) Hardness−indentation depth ($H - h$) relationship for Ni-based single-crystal superalloys. (**b**) Plot of H^2 versus h^{-1} with experimental data, where the red dash line represents the Nix–Gao model fit, while the blue one corresponds to the modified Nix–Gao model, accounting for the Ni_3Al/Ni interfacial contribution.

4.3. Molecular Dynamics Simulations

To clarify the role of the Ni_3Al/Ni interface, molecular dynamics simulations were performed with indentation sites positioned at the Ni_3Al precipitate, Ni matrix, and Ni_3Al/Ni interface. Here, it is worth noting that, in these simulations, the Ni matrix represents the center of the Ni_3Al/Ni interface in experiments. Dislocation activities were tracked to correlate the microstructural evolution with indentation force and hardness profiles. As shown in Figure 8, for a given indentation depth, indentation at the Ni_3Al precipitate yields the highest force and hardness values, while indentation at the Ni matrix shows the lowest, with values at the Ni_3Al/Ni interface falling between. This trend aligns with the experimental results. Additionally, force and hardness exhibit fluctuations during indentation, corresponding to the pop-in events observed in nanoindentation experiments.

For further comparison, microstructures of these three indentation sites at a depth of 4.0 nm are shown in Figure 9a–c. When indentation occurs on the Ni_3Al precipitate, the Ni_3Al/Ni interface effectively restricts the propagation of dislocations from Ni_3Al into the Ni matrix, as most dislocations remain localized within the Ni_3Al precipitate. Additionally, the interfacial misfit dislocation network at the Ni_3Al/Ni interface contacts towards the interface center compared to its initial state (see insets in Figure 9a), which further impedes dislocation movement.

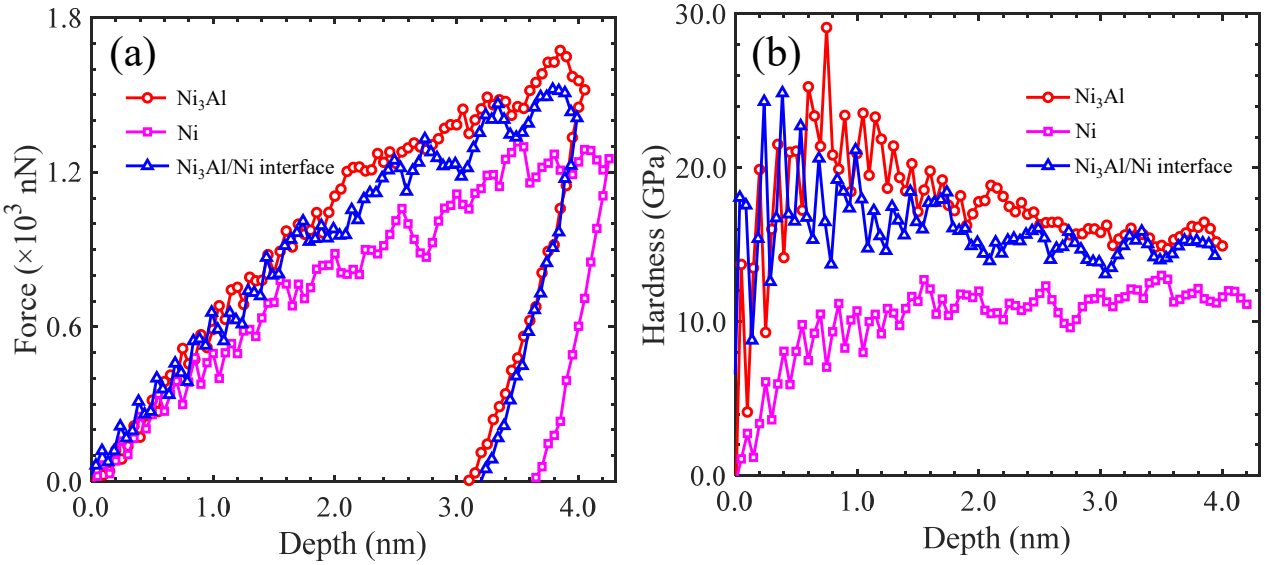


Figure 8. Results of molecular dynamics simulations for nanoindentation. (**a**) Indentation force–depth curves and (**b**) hardness–depth relationships for indentation sites at the Ni_3Al precipitate, Ni matrix, and Ni_3Al/Ni interface.

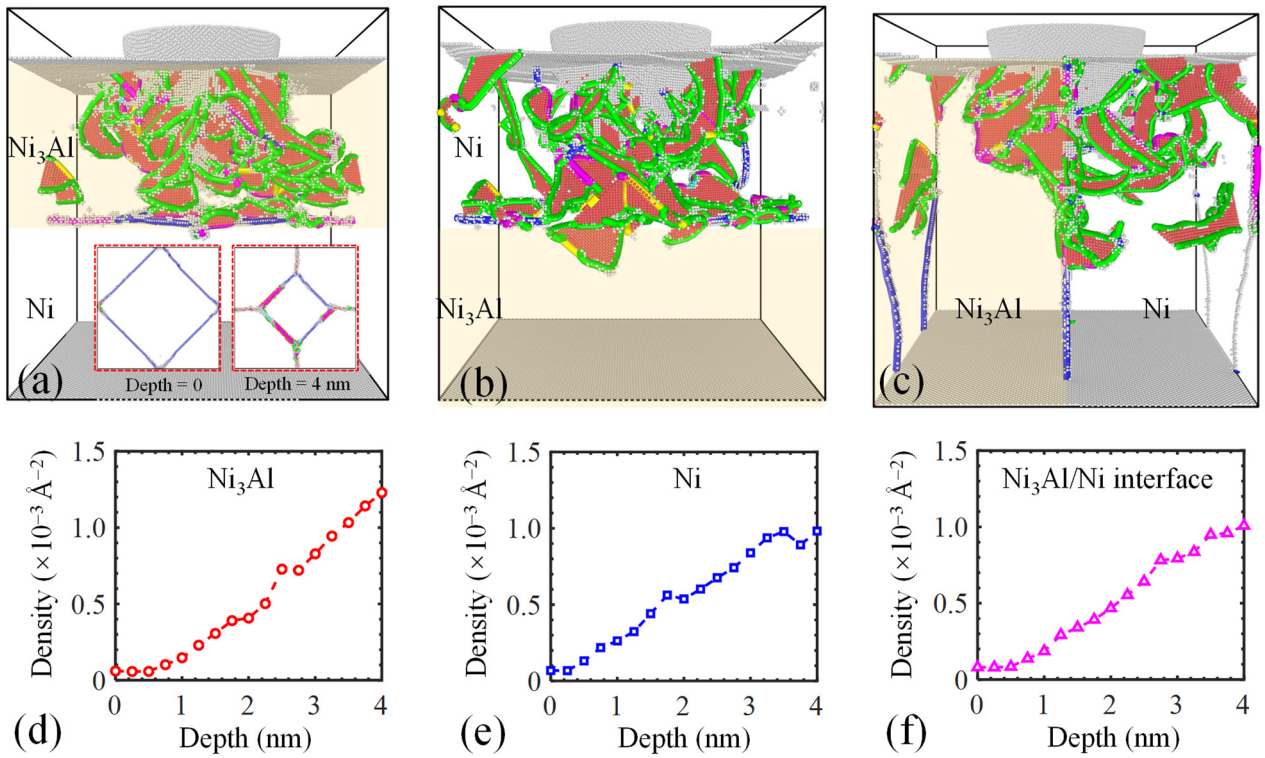


Figure 9. Atomic configurations and microstructural evolution at a maximum indentation depth of 4.0 nm, with indentation sites at (**a**) Ni_3Al precipitate, (**b**) Ni matrix, and (**c**) Ni_3Al/Ni interface. Dislocation analysis is used to illustrate the microstructural evolution, with the following colors and symbols indicating different dislocation types: green for 1/6<112> Shockley, blue for 1/2<110> perfect, purple for 1/6<110> stair-rod, yellow for 1/3<100> Hirth, and red for other dislocations. For clarity, FCC structures were removed from images (**a**) to (**c**); (**d**–**f**) show changes in dislocation density with indentation depth for indentation sites at the Ni_3Al precipitate, Ni matrix, and Ni_3Al/Ni interface, respectively.

As shown in Figure 9b, indentation on the Ni matrix results in a more dispersed dislocation distribution. Dislocations generated beneath the indenter extend towards and interact with the interfacial misfit dislocation network at the Ni_3Al/Ni interface, disturbing its structure and partially shearing into the Ni_3Al precipitate.

When the Ni_3Al/Ni interface is directly indented, the interfacial misfit dislocation network quickly deviates from its initial quadrilateral arrangement due to interactions with dislocations generated under the indenter. Dislocations then spread across both the Ni matrix and Ni_3Al precipitate, accumulating predominantly at the interface, where they are absorbed and pinned (Figure 9c).

As shown in Figure 9d–f, the dislocation density increases with indentation depth, reaching its highest value at the Ni_3Al precipitate and its lowest at the Ni matrix at a depth of 4 nm. As expected, the Ni_3Al/Ni interface shows an intermediate dislocation density under direct indentation.

5. Discussion

The indentation force–depth curves show that all samples initially undergo elastic deformation, followed by plastic deformation characterized by an obvious displacement burst, or pop-in events [37]. Two types of pop-in events are identified in the loading sequence, which is consistent with experimental observations in other metallic materials [38]. The first pop-in event precisely corresponds to the peak on a hardness–depth curve. Both experiments and simulations unveil that, at comparable indentation depths, the highest hardness occurs when indenting the Ni_3Al precipitate, while the lowest hardness is observed in the Ni matrix. Simulations also show that dislocation activities are confined within the Ni_3Al precipitate, offering a high dislocation density that contributes to increased hardness. Additionally, the simulations highlight the role of the Ni_3Al/Ni interface in dislocation annihilation and obstruction, consistent with previous studies [20,21].

The fluctuation in hardness at indentation depths below 100 nm is attributed to variation in indentation sites, which can include the Ni_3Al precipitate, Ni matrix, or Ni_3Al/Ni interface. As indentation depth increases, this fluctuation lessens as the indentation area expands to encompass all three regions, thereby reflecting the response of the entire superlattice structure of Ni-based single-crystal superalloys. Therefore, as shown in Figure 7b, the indentation size effect at depths beyond 70 nm is well depicted by the Nix–Gao model [11]:

$$H = H_0\sqrt{1+\frac{h^*}{h}}, \tag{6}$$

where H_0 and h^* are the macroscopic hardness and characteristic depth, respectively. As shown in Figure 7b, H_0 and h^* are 6.4 GPa and 95.9 nm, respectively, by fitting the data with indentation depths from 70 to 400 nm. However, below 70 nm, there is an apparent deviation between experimental data and the Nix–Gao model.

As is known, the macroscopic hardness in Equation (6) is related to the statistically stored dislocation density calculated by

$$H_0 = 3\sqrt{3}\alpha G b\sqrt{\rho_s}, \tag{7}$$

where α is a constant, G is the shear modulus, b is the magnitude of Burgers vector, and ρ_s is the statistically stored dislocation density. Based on Equation (7), it is obvious that, due to the high dislocation density in the Ni_3Al precipitate, it results in the largest hardness (see Figures 8 and 9). The characteristic depth in Equation (6) can be calculated by

$$h^* = \frac{81}{2}b\alpha^2\tan^2\theta\left(\frac{G}{H_0}\right)^2, \tag{8}$$

where θ is the angle between the surface of a conical indenter and the indented plane. For a given material and an indenter geometry, h^* depends on the statistically stored dislocation

density through H_0 [6,9,13,16]. Therefore, to apply the Nix–Gao model at indentation depths below 70 nm, Equation (6) can be modified as

$$H = H_0\sqrt{1 + \frac{h^*}{h} - \left(\frac{h^{\mathrm{I}}}{h}\right)^2}, \tag{9}$$

where h^{I} is a modifying factor that accounts for the Ni_3Al/Ni interfacial contribution. As shown in Figure 7b, the experimental data for indentation depths from 30 to 400 nm can be fitted by Equation (9) with the parameters H_0 = 6.1 GPa, h^* = 143.0 nm, and h^{I} = 50.8 nm. Therefore, by considering the Ni_3Al/Ni interfacial contribution, the indentation size effect of Ni-based single-crystal superalloys can be accurately described by the modified Nix–Gao model.

6. Conclusions

To investigate the indentation size effect at very shallow depths (<100 nm), a series of nanoindentation experiments and molecular dynamics simulations were conducted on Ni-based single-crystal superalloys. This study examined the indentation size effect and mechanical behaviors, focusing on the contributions from the Ni_3Al/Ni interface. The main conclusions are summarized as follows:

(1) For indentation depths under 100 nm, hardness varies significantly with indentation sites. The closer the indentation site is to the Ni_3Al/Ni interface, the lower the hardness observed, highlighting the influence of the Ni_3Al/Ni interface on material hardness.
(2) Molecular dynamic simulations show that the Ni_3Al/Ni interfacial misfit dislocation networks can effectively absorb and hinder dislocations. The observed site-dependent hardness arises from a lower dislocation density at the center of the Ni_3Al/Ni interface during indentation.
(3) By incorporating the Ni_3Al/Ni interfacial contribution, the indentation size effect is well-captured across indentation depths from 30 to 400 nm using a modified Nix–Gao model.

It is expected that these findings will provide new insights into the indentation size effect and deformation mechanisms of Ni-based single-crystal superalloys, potentially enhancing their applications in the aerospace industry.

Author Contributions: Z.Z.: conceptualization, investigation, methodology, data curation, writing—original draft, funding acquisition. X.Z.: writing—review and editing, funding acquisition. R.Y.: writing—review and editing, funding acquisition. J.W.: conceptualization, supervision, writing—review and editing. C.L.: writing—review and editing. All authors have read and agreed to the published version of the manuscript.

Funding: This work has been supported by the National Natural Science Foundation of China (Grant Nos. 12302241 and 12325205), the Natural Science Foundation of Gansu Province of China (Grant Nos. 23JRRA1118 and 23ZDKA0009), and the Strategic Priority Research Program of the Chinese Academy of Sciences (Project No. XDB0620101).

Data Availability Statement: The data that support the findings within this paper are available from the corresponding authors upon reasonable request.

Acknowledgments: The simulations were performed on resources provided by the Supercomputing Center of Lanzhou University and the Pawsey Supercomputing Research Center with funding from the Australian Government and the Government of Western Australia.

Conflicts of Interest: The authors declare that they have no known competing financial interests or personal relationships that could have appeared to influence the work reported in this paper.

References

1. Nili, H.; Kalantar-Zadeh, K.; Bhaskaran, M.; Sriram, S. In situ nanoindentation: Probing nanoscale multifunctionality. *Prog. Mater. Sci.* **2012**, *58*, 1–29. [CrossRef]
2. Shuang, F.; Wang, B.; Aifantis, K. Revealing multiple strengthening transitions in crystalline-amorphous nanolaminates through molecular dynamics. *Mater. Today Commun.* **2023**, *35*, 105675. [CrossRef]
3. Shuang, F.; Dai, Z.H.; Aifantis, K.E. Strengthening in metal/graphene composites: Capturing the transition from interface to precipitate hardening. *ACS Appl. Mater. Interfaces* **2021**, *12*, 26610–26620. [CrossRef]
4. Zhou, P.; Shuang, F.; Shi, R.-H. Distinct nucleation and propagation of prismatic dislocation loop arrays in Ni and medium-entropy CrCoNi alloy: Insights from molecular dynamics simulations. *Mater. Today Commun.* **2023**, *36*, 106791. [CrossRef]
5. Milman, Y.V.; Golubenko, A.A.; Dub, S.N. Indentation size effect in nanohardness. *Acta Mater.* **2011**, *59*, 7480–7487. [CrossRef]
6. Ma, X.; Higgins, W.; Liang, Z.; Zhao, D.; Pharr, G.M.; Xie, K.Y. Exploring the origins of the indentation size effect at submicron scales. *Proc. Natl. Acad. Sci. USA* **2021**, *118*, e2025657118. [CrossRef]
7. Li, X.; Liang, J.; Shi, T.; Yang, D.; Chen, X.; Zhang, C.; Liu, Z.; Liu, D.; Zhang, Q. Tribological behaviors of vacuum hot-pressed ceramic composites with enhanced cyclic oxidation and corrosion resistance. *Ceram. Int.* **2020**, *46*, 12911–12920. [CrossRef]
8. Li, X.; Shi, T.; Li, B.; Chen, X.; Zhang, C.; Guo, Z.; Zhang, Q. Subtractive manufacturing of stable hierarchical micro-nano structures on AA5052 sheet with enhanced water repellence and durable corrosion resistance. *Mater. Des.* **2019**, *183*, 108152. [CrossRef]
9. Swadener, J.G.; George, E.P.; Pharr, G.M. The correlation of the indentation size efect measured with indenters of various shapes. *J. Mech. Phys. Solids* **2002**, *50*, 681–694. [CrossRef]
10. Qu, S.; Huang, Y.; Pharr, G.; Hwang, K. The indentation size effect in the spherical indentation of iridium: A study via the conventional theory of mechanism-based strain gradient plasticity. *Int. J. Plast.* **2005**, *22*, 1265–1286. [CrossRef]
11. Nix, W.D.; Gao, H. Indentation size effects in crystalline materials: A law for strain gradient plasticity. *J. Mech. Phys. Solids* **1998**, *46*, 411–425. [CrossRef]
12. Elmustafa, A.A.; Stone, D.S. Nanoindentation and the indentation size efect: Kinetics of deformation and strain gradient plasticity. *J. Mech. Phys. Solids* **2003**, *51*, 357–381. [CrossRef]
13. Shim, S.; Bei, H.; George, E.; Pharr, G. A different type of indentation size effect. *Scr. Mater.* **2008**, *59*, 1095–1098. [CrossRef]
14. Sangwal, K. On the reverse indentation size effect and microhardness measurement of solids. *Mater. Chem. Phys.* **2000**, *63*, 145–152. [CrossRef]
15. Qu, S.; Huang, Y.; Nix, W.; Jiang, H.; Zhang, F.; Hwang, K. Indenter tip radius effect on the Nix–Gao relation in micro- and nanoindentation hardness experiments. *J. Mater. Res.* **2004**, *19*, 3423–3434. [CrossRef]
16. Durst, K.; Backes, B.; Göken, M. Indentation size effect in metallic materials: Correcting for the size of the plastic zone. *Scr. Mater.* **2005**, *52*, 1093–1097. [CrossRef]
17. Feng, G.; Nix, W.D. Indentation size effect in MgO. *Scr. Mater.* **2004**, *51*, 599–603. [CrossRef]
18. Zhang, Z.W.; Fu, Q.; Wang, J.; Xiao, P.; Ke, F.J.; Lu, C.S. Hardening Ni_3Al via complex stacking faults and twinning boundary. *Comput. Mater. Sci.* **2021**, *188*, 110201. [CrossRef]
19. Dai, K.; Zhang, C.; Li, J. Shear banding suppression in Cu/TiZrNb nanolayered composites through dual crystalline/amorphous interfaces. *Mater. Today Commun.* **2024**, *38*, 108481. [CrossRef]
20. Zhang, Z.; Fu, Q.; Wang, J.; Yang, R.; Xiao, P.; Ke, F.; Lu, C. Atomistic modeling for the extremely low and high temperature-dependent yield strength in a Ni-based single crystal superalloy. *Mater. Today Commun.* **2021**, *27*, 102451. [CrossRef]
21. Zhang, Z.; Fu, Q.; Wang, J.; Yang, R.; Xiao, P.; Ke, F.; Lu, C. Interaction between the edge dislocation dipole pair and interfacial misfit dislocation network in Ni-based single crystal superalloys. *Int. J. Solids Struct.* **2021**, *228*, 111128. [CrossRef]
22. Wang, Y.; Dai, K.; Lu, W.; Chen, S.; Li, J. Remarkable strengthening of nanolayered metallic composites by nanoscale crystalline interfacial layers. *Mater. Today Commun.* **2024**, *39*, 108809. [CrossRef]
23. Du, Y.; Hu, H.; Yuan, X.; Long, M.; Chen, D. Novel insights into interstitial atoms synergistically augmenting the mechanical characteristics of NiCo coating and interfacial strength with Cu substrate. *J. Alloys Compd.* **2024**, *983*, 173728. [CrossRef]
24. Du, Y.; Chen, Y.; Yuan, X.; Liu, P.; Long, M.; Chen, D. Potential mechanisms of interstitial atomic enhancement and interface failure behavior in Ni_3Co/Cu systems. *Appl. Surf. Sci.* **2023**, *629*, 157388. [CrossRef]
25. Wan, K.; He, J.; Shi, X. Construction of High Accuracy Machine Learning Interatomic Potential for Surface/Interface of Nanomaterials—A Review. *Adv. Mater.* **2023**, *36*, e2305758. [CrossRef]
26. Zhang, Z.; Cai, W.; Feng, Y.; Duan, G.; Wang, J.; Wang, J.; Yang, R.; Xiao, P.; Ke, F.; Lu, C. Dislocation reactions dominated pop-in events in nanoindentation of Ni-based single crystal superalloys. *Mater. Charact.* **2023**, *200*, 112883. [CrossRef]
27. Han, Q.-N.; Rui, S.-S.; Qiu, W.; Su, Y.; Ma, X.; Su, Z.; Cui, H.; Shi, H. Effect of crystal orientation on the indentation behaviour of Ni-based single crystal superalloy. *Mater. Sci. Eng. A* **2020**, *773*, 138893. [CrossRef]
28. Li, X.; Bhushan, B. A review of nanoindentation continuous stiffness measurement technique and its applications. *Mater. Charact.* **2002**, *48*, 11–36. [CrossRef]
29. Voter, A.F.; Chen, S.P. Accurate Interatomic Potentials for Ni, Al and Ni3Al. *MRS Proc.* **1986**, *82*, 175. [CrossRef]
30. Tian, S.G.; Zhou HHZhang, J.H.; Yang, H.C.; Xu, Y.B.; Hu, Z.Q. Formation and role of dislocation networks during high temperature creep of a single crystal nickelbase superalloy. *Mater. Sci. Eng. A* **2000**, *279*, 160–165.
31. Plimpton, S. Fast Parallel Algorithms for Short-Range Molecular Dynamics. *J. Comput. Phys.* **1995**, *117*, 1−19. [CrossRef]
32. Mishin, Y. Atomistic modeling of the γ and γ′-phases of the Ni−Al system. *Acta Mater.* **2004**, *52*, 1451–1467. [CrossRef]

33. Amodeo, J.; Begau, C.; Bitzek, E. Atomistic simulations of compression tests on Ni_3Al nanocubes. *Mater. Res. Lett.* **2014**, *2*, 140–145. [CrossRef]
34. Yan, Y.; Zhou, S.; Liu, S. Atomistic simulation on nanomechanical response of indented graphene/nickel system. *Comput. Mater. Sci.* **2017**, *130*, 16–20. [CrossRef]
35. Peng, P.; Liao, G.; Shi, T.; Tang, Z.; Gao, Y. Molecular dynamic simulations of nanoindentation in aluminum thin film on silicon substrate. *Appl. Surf. Sci.* **2010**, *256*, 6284–6290. [CrossRef]
36. Stukowski, A. Visualization and analysis of atomistic simulation data with OVITO—The Open Visualization Tool. *Model. Simul. Mater. Sci. Eng.* **2010**, *18*, 015012. [CrossRef]
37. Sato, Y.; Shinzato, S.; Ohmura, T.; Hatano, T.; Ogata, S. Unique universal scaling in nanoindentation pop-ins. *Nat. Commun.* **2020**, *11*, 4177. [CrossRef]
38. Voyiadjis, G.Z.; Yaghoobi, M. Review of Nanoindentation Size Effect: Experiments and Atomistic Simulation. *Crystals* **2017**, *7*, 321. [CrossRef]

Disclaimer/Publisher's Note: The statements, opinions and data contained in all publications are solely those of the individual author(s) and contributor(s) and not of MDPI and/or the editor(s). MDPI and/or the editor(s) disclaim responsibility for any injury to people or property resulting from any ideas, methods, instructions or products referred to in the content.